Somayeh Abdi, Matthias Bönisch, Steffen Oswald, Mohsen Samadi Khoshkhoo, Wolfgang Gruner, Martina Lorenzetti, Ulrike Wolff, Mariana Calin, Jürgen Eckert, Annett Gebert

Thermal oxidation behavior of glass-forming Ti–Zr–(Nb)–Si alloys

Erstveröffentlichung in / First published in:

Journal of materials research. 2016, 31 (9), S. 1264 – 1274 [Zugriff am: 15.04.2020]. Cambridge University Press. ISSN 2044-5326.

DOI: https://doi.org/10.1557/jmr.2016.122

Thermal oxidation behavior of glass-forming Ti–Zr–(Nb)–Si alloys

Somayeh Abdi
Leibniz-Institute for Solid State and Materials Research IFW Dresden, D-01171 Dresden, Germany

Matthias Bönisch[a)]
Leibniz-Institute for Solid State and Materials Research IFW Dresden, D-01171 Dresden, Germany; and TU Dresden, Institute of Structural Physics, D-01069 Dresden, Germany

Steffen Oswald, Mohsen Samadi Khoshkhoo,[b)] and Wolfgang Gruner
Leibniz-Institute for Solid State and Materials Research IFW Dresden, D-01171 Dresden, Germany

Martina Lorenzetti
Department for Nanostructured Materials, Jožef Stefan Institute, 1000 Ljubljana, Slovenia

Ulrike Wolff, Mariana Calin, Jürgen Eckert,[c),d)] and Annett Gebert
Leibniz-Institute for Solid State and Materials Research IFW Dresden, D-01171 Dresden, Germany

(Received 16 December 2015; accepted 7 March 2016)

The glass-forming $Ti_{75}Zr_{10}Si_{15}$ and $Ti_{60}Zr_{10}Nb_{15}Si_{15}$ alloys composed of nontoxic elements may represent new materials for biomedical applications. For this study, melt-spun alloy samples exhibiting glass–matrix nanocomposite structures were subjected to thermal oxidation treatments in synthetic air to improve their surface characteristics. 550 °C was identified as the most appropriate temperature to carry out oxidative surface modifications while preserving the initial metastable microstructure. The modified surfaces were evaluated considering morphological and structural aspects, and it was found that the oxide films formed at 550 °C are amorphous and consist mainly of TiO_2; their thicknesses were estimated to be ~560 nm for $Ti_{75}Zr_{10}Si_{15}$ and ~460 nm for $Ti_{60}Zr_{10}Nb_{15}Si_{15}$. The thermally treated sample surfaces exhibit not only higher roughnesses and higher hardnesses but also improved wettability compared to the as-spun materials. By immersion of oxidized samples in simulated body fluid Ca- and P-containing coatings exhibiting typical morphologies of apatite are formed.

I. INTRODUCTION

Glass-forming Ti-based alloys are considered as potential new materials for implant applications especially due to their superior mechanical properties in comparison with their crystalline counterparts, i.e., higher strength, lower Young's modulus as well as high wear resistance.[1–4] They can exhibit high corrosion resistance in physiological environments when their composition is free of corrosive, cytotoxic, or allergenic elements like Ni or Cu.[5,6]

Considering these aspects, glass-forming $Ti_{75-x}Zr_{10}Nb_xSi_{15}$ (x = 0, 15) alloys appear to be very prospective. They comprise only nontoxic elements, yet as their particular compositions yield only a limited glass forming ability their potential application is restricted to coatings for orthopedic implants that require very high wear and corrosion resistance. Rapidly quenched ribbons of these alloys exhibit a nanocomposite structure comprising a glass-matrix and embedded single β-Ti nanocrystals.[7] Analysis of the mechanical properties revealed a combination of high hardness (H) and low reduced elastic modulus (E_r) resulting in high wear resistance. Ribbon samples of both alloys exhibited a hardness of 8–10 GPa and a reduced elastic modulus of about 108–123 GPa. Thus, the elastic modulus of these nanocomposites is comparable to that of commercial crystalline reference materials such as cp-Ti and Ti–6A–l4V.[7] Yet, the hardness of the ribbon samples is about three times higher than the hardness of the commercial reference materials. The very high hardness values, combined with the moderate elastic modulus values, imply a high wear resistance of the $Ti_{75-x}Zr_{10}Nb_xSi_{15}$ (x = 0, 15) nanocomposites. The corrosion and passivation behavior of $Ti_{75}Zr_{10}Si_{15}$ and $Ti_{60}Zr_{10}Nb_{15}Si_{15}$

Contributing Editor: Eric A. Stach
[a)]Address all correspondence to this author.
e-mail: m.boenisch@ifw-dresden.de
[b)]Current address: Carl Zeiss Microscopy GmbH, Carl-Zeiss-Strasse 22, 73,447 Oberkochen, Germany.
[c)]Current address: Erich Schmid Institute of Materials Science, Austrian Academy of Sciences (ÖAW) and Department Materials Physics, Montanuniversität Leoben, Jahnstraβe 12, A-8700 Leoben, Austria.
[d)]This author was an editor of this journal during the review and decision stage. For the *JMR* policy on review and publication of manuscripts authored by editors, please refer to http://www.mrs.org/jmr-editor-manuscripts/.
A previous error in this article has been corrected, see 10.1557/jmr.2016.192.
DOI: 10.1557/jmr.2016.122

alloys in simulated body fluid (SBF, Ringer solution) at 37 °C was assessed, and a high stability of their passive states without any indication for pitting was evidenced.[6]

Generally, the high corrosion resistance of Ti-based implant materials arises from a spontaneous surface oxide film formation (mainly TiO_2) which protects the material from biologically relevant environments.[8] This very smooth and mostly amorphous film is defined as bioinert and therefore, Ti-based material surfaces cannot easily bond to bone tissue. They are encapsulated after implantation by fibrous tissues which isolate them from the surrounding bone.[9] As a consequence, this may result in loosening of the implant after long-term resorption of bone tissue. Furthermore, the poor mechanical properties of this native oxide can lead to fracture of the film (typical thickness about 4–6 nm) under very low stresses such as by rubbing the implant against soft tissues,[10] and the healing of the passive oxide layer causes gradual consumption of the bulk material.[11] Besides, the release of wear debris and metal ions can lead to adverse tissue reactions.[12]

Therefore, surface modifications are applied to change the material surface composition, structure, and morphology to improve the chemical bonding and/or mechanical anchoring between bone and material.[9,13,14]

Thermal oxidation is one of the most efficient surface modification techniques to generate a thicker barrier-type oxide layer on a Ti-based material surface and is an established method to improve commercial bone implant surfaces towards higher bioactivity.[15,16] During a thermal oxidation process Ti can easily react with air due to its very high affinity to oxygen. This induces the formation of a thicker oxide layer with temperature- and time-dependent grain size and morphology of the usually crystalline oxides. Consequently, surface roughness, hardness, corrosion, and wear resistance can increase.[10,15,17–20] The increase of the surface roughness can improve the surface wettability and thus, provide better cell adhesion. Higher wettability enhances cellular response through improved protein absorption and apatite formation.[21] Moreover it was demonstrated that the crystalline forms of TiO_2, like anatase or rutile, improve the bioactivity and the implant osseointegration in vivo.[22,23]

In this study, a fundamental thermal oxidation analysis has been conducted for glass–matrix nanocomposite $Ti_{75}Zr_{10}Si_{15}$ and $Ti_{60}Zr_{10}Nb_{15}Si_{15}$ alloys produced by melt-spinning. Firstly, the temperature- and time-dependent behaviors were generally assessed under inert gas atmosphere and in synthetic air to determine the suitable thermal regime for effective surface oxide formation without crystallization of the metastable alloy state. Secondly, a detailed characterization of the oxide films formed under these conditions was conducted and related effects on implant specific properties like hardness, wettability, and apatite-forming ability were evaluated.

II. MATERIALS AND METHODS

A. Materials

Ingots with nominal compositions of $Ti_{75}Zr_{10}Si_{15}$ and $Ti_{60}Zr_{10}Nb_{15}Si_{15}$ were produced by arc-melting of pure elements in a highly purified Ar atmosphere. Ribbons with 30–50 μm thickness and 3–4 mm width were prepared by melt-spinning in an Ar atmosphere using a single-roller Cu-wheel at a rotation speed of 35 m/sec. The rapid quenching process was started from a melt temperature of 1720 °C. Details of sample preparation and microstructural characterization are given in Ref. 7. The $Ti_{75}Zr_{10}Si_{15}$ and $Ti_{60}Zr_{10}Nb_{15}Si_{15}$ melt-spun ribbons were used as substrate materials for further thermal oxidation treatments. The ribbons were cut to samples of equal dimensions (3–4 mm width and 2 cm length) and were cleaned once in ethanol and twice in de-ionized water for 10 min each in an ultrasonic bath (VWR International, Leuven).

B. Thermal oxidation analysis

The fundamental thermal properties of the rapidly quenched alloy samples were examined by means of differential scanning calorimetry (DSC) in purified Ar atmosphere. For this, experiments with a DSC-7 device (Perkin Elmer Inc., Waltham, Massachusetts) were conducted at a constant heating rate of 10 °C/min.

Thermal oxidation studies of sample strips standing upright in a ceramic crucible were carried out by thermogravimetric analysis (TGA) using a STA 449C Jupiter device model (NETZSCH Group, Selb, Germany). The atmosphere was high-purity synthetic air with a constant net flow rate of 50 mL/min. For dynamic TGA, the samples were continuously heated in a furnace with a constant heating rate of 10 °C/min. For isothermal TGA studies a four step procedure was followed. It started with initial fast dynamic heating with 40 °C/min up to a temperature of 100 °C below the isothermal annealing temperature. This was followed by slower dynamic heating with 10 °C/min up to the isothermal annealing temperature. Isothermal annealing was conducted at selected temperatures for 3 h. Finally, a cooling step was carried out with a cooling rate of about 40 °C/min.

C. Materials characterization and surface state analysis

The phase constituents of samples thermally treated at different temperatures were identified by x-ray diffraction (XRD) using a D3290 X'pert PRO device (PANalytical, Almelo, The Netherlands) with Co-Kα radiation. The surface morphology was evaluated by high resolution scanning electron microscopy (HR-SEM, Leo Gemini 1530 microscope). The thicknesses of the oxide layers as well as their microstructures were assessed by

transmission electron microscopy (TEM) using a Tecnai F30 microscope (FEI Company, Hillsboro, Oregon) operated at 300 kV. Atomic force microscopy (AFM) was conducted to measure the surface roughness of the as-spun and thermally treated $Ti_{75}Zr_{10}Si_{15}$ and $Ti_{60}Zr_{10}Nb_{15}Si_{15}$ ribbons using a Dimension 3100 AFM (Veeco Instrument Inc., Plainview, New York).

For detailed compositional characterization of heat-influenced surface regions of the oxidized samples Auger electron spectroscopy (AES) sputter depth-profiling was conducted. A JAMP 9500 F Field Emission Microprobe (JEOL Ltd., Tokyo, Japan) was used which was equipped with a hemispherical analyzer with electron beam conditions of 10 keV and 10 nA. A scanned beam of Ar^+ ions of 2 keV with a scan size of around 1 mm × 1 mm was applied which resulted in sputtering rates of 6.6 nm/min and 17 nm/min (determined for silicon oxide). A semiquantitative correction in the depth profiles was done, details are described in Ref. 24.

The Vickers microhardness was measured on the surface of as-spun and thermally oxidized ribbons using a HVM-2000 microhardness tester (Shimadzu Corporation, Kyoto, Japan). 30 indents with a constant applied load of 10 g and a holding time of 10 s were placed randomly across the sample surface and the mean value, and standard deviation was calculated.

The water wettability of selected sample surfaces was determined by sessile drop contact angles measurements using a Theta Lite T101 optical tensiometer (Attension - Biolin Scientific, Stockholm, Sweden). Four droplets of distilled water were placed at different positions on each sample (airside of the ribbons) at room temperature and the average value was taken as contact angle measure and is presented as mean value and standard deviation.

D. SBF tests

The ability for hydroxyapatite formation on surfaces of $Ti_{75}Zr_{10}Si_{15}$ and $Ti_{60}Zr_{10}Nb_{15}Si_{15}$ ribbons was examined in a SBF. The SBF solution was prepared according to Kokubo and Takadama[25] with the chemical composition of NaCl (7.92 g/L), $NaHCO_3$ (0.356 g/L), KCl (0.376 g/L), $Na_2HPO_4{\cdot}3H_2O$ (0.147 g/L), $MgCl_2{\cdot}6H_2O$ (0.309 g/L), 1 M HCl (15 mL), $CaCl_2$ (0.375 g/L), Na_2SO_4 (0.162 g/L), Tris (6.12 g/L). Before immersion, samples were cleaned ultrasonically in EtOH for 15 min, dried at 100 °C and then treated in 10 M NaOH at 60 °C for 24 h to alkalize the surface. Subsequently, the samples were cleaned with bi-distilled water for a short time and dried for 24 h at room temperature.[26] They were immersed in the SBF solution at 37 °C for 10 and 20 days. Finally, they were cleaned three times with bi-distilled water and dried for 24 h at room temperature. After this treatment, the morphologies of the sample surfaces were investigated with scanning electron microscopy (SEM) and the chemical composition was assessed with energy-dispersive x-ray spectroscopy (EDX).

III. RESULTS AND DISCUSSION

Melt-spun ribbons produced by rapid quenching of the melt from a temperature of 1720 °C were used for this study. It has been shown that the ribbons of the $Ti_{75}Zr_{10}Si_{15}$ and $Ti_{60}Zr_{10}Nb_{15}Si_{15}$ alloys exhibit a nanocomposite structure of single β-Ti nanocrystals embedded in a glassy matrix and the underlying phase reactions have been discussed (all details in Refs. 5 and 7).

A. Thermal stability of melt-spun ribbons

DSC measurements have been conducted to study the crystallization behavior of the melt-spun ribbons under inert gas atmosphere. Figure 1 shows characteristic DSC curves of $Ti_{75}Zr_{10}Si_{15}$ and $Ti_{60}Zr_{10}Nb_{15}Si_{15}$ samples. For both alloys, no glass transition (T_g) is detectable, but two exothermic peaks originating from crystallization, a first weak one and a second very pronounced one, are observed. The onsets of the first and the second crystallization peaks are T_{x1} = 457 °C, T_{x2} = 590 °C for $Ti_{75}Zr_{10}Si_{15}$ and T_{x1} = 472 °C, T_{x2} = 632 °C for $Ti_{60}Zr_{10}Nb_{15}Si_{15}$ samples.

Further heating treatments up to temperatures slightly above the two exothermic peaks of the $Ti_{60}Zr_{10}Nb_{15}Si_{15}$ alloy were exemplarily done to identify the associated phase reactions. The XRD patterns and TEM results are summarized in Ref. 5 and reveal a composite structure consisting of nanosized spherical particles dispersed in a glassy matrix for a sample heated up to 590 °C. Therefore, it can be concluded that the first weak

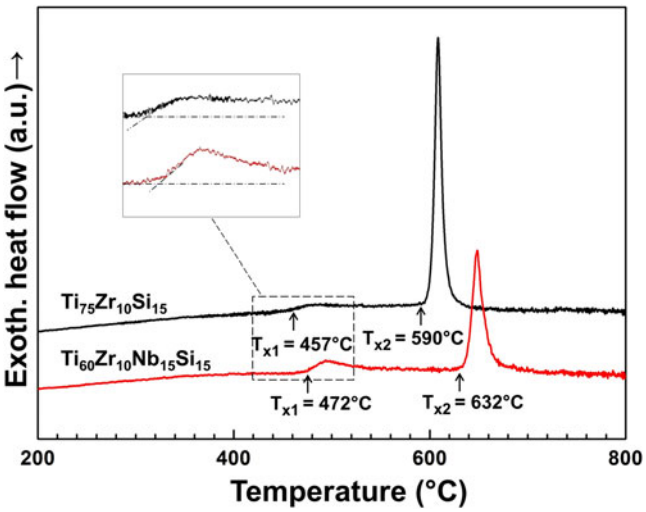

FIG. 1. DSC curves of $Ti_{75}Zr_{10}Si_{15}$ and $Ti_{60}Zr_{10}Nb_{15}Si_{15}$ melt-spun ribbons recorded at a constant heating rate of 10 °C/min in argon atmosphere.

exothermic peak is associated with the triggering of the formation and growth of bcc β-Ti(Nb) nanocrystals embedded in a residual glassy matrix as a primary crystallization phase. The formation of bcc nanocrystals may be due to "quenched-in" nuclei which are not bypassed during the melt-spinning and which can act as heterogeneous nucleation sites during subsequent heating. For a sample heated up to 720 °C, the formation of a multiphase ultrafine crystalline structure at nanosize level was detected comprising the intermetallic phase $(Ti,Zr,Nb)_5Si_3$ and the bcc β-Ti(Nb) phase (the same phases as those identified in the cast crystalline counterpart, details in Ref. 7).

It is noticeable from the XRD results that for the quaternary alloy, the main crystallization process occurs at higher temperatures than for the ternary alloy. As described by Calin et al.,[5] the addition of the β-stabilizer Nb results in primary nanocrystallization of the bcc β-Ti (Nb) phase with a high particle density upon heat treatment in inert atmosphere. The high particle density may cause rapid diffusion impaction which inhibits nanocrystal growth. In addition, Si has a reduced solid solubility in the bcc β-Ti(Nb) phase and the rejection of it at the nanocrystal-amorphous matrix interface may delay the nucleation of secondary intermetallic phases.

In conclusion, the onset temperatures of the second crystallization peaks represent the maximum temperatures up to which the main fractions of the amorphous matrix phase are stable for each alloy composition.

B. Thermal oxidation of melt-spun ribbons

TGA has been applied to investigate the oxidation behavior of the alloys in a synthetic air environment.

Both dynamic and isothermal TGA methods were used. Figure 2 displays characteristic dynamic TGA curves of $Ti_{75}Zr_{10}Si_{15}$ and $Ti_{60}Zr_{10}Nb_{15}Si_{15}$ ribbons recorded at a continuous heating rate of 10 °C/min. Both curves can be divided into 4 regions according to their trend. The first region (I) reaches up to 400 °C. There, no significant mass change can be observed, which indicates that no noteworthy oxidation occurs, yet. The second region (II) spans from 400 °C to 650 °C and is characterized by a gradual increase in mass, which indicates the beginning of oxidation processes with rising temperature. At the higher temperature level of this second region, the surface oxidation superimposes the main crystallization events as indicated by the second sharp exothermic peaks in the DSC curves of Fig. 1. Obviously, internal intermetallic transformation triggers the surface oxidation. Therefore, there is a short third region (III) ranging from ~650 °C to ~720 °C in which the slope of the mass change curve diminishes. The last region (IV) of the mass change curves measured up to 1000 °C is characterized by a sharp increase of the slope for the $Ti_{75}Zr_{10}Si_{15}$ alloy and a less pronounced increase for the $Ti_{60}Zr_{10}Nb_{15}Si_{15}$ alloy. Nevertheless, both are indicative for enhanced oxidation. Comparing the response of the ternary alloy with that of the quaternary one, it can be concluded that addition of Nb to the alloy results in a decreasing oxidation rate. This can be seen in relation to the earlier described effect of Nb on improving the passive film stability at room temperature.[27]

To understand the oxidation behavior in more detail, isothermal measurements have been carried out in synthetic air at selected temperatures and those samples were subjected to further characterization. The temperatures for the isothermal annealing tests have been selected from regions II, III, and IV of the dynamic TGA curves shown in Fig. 2.

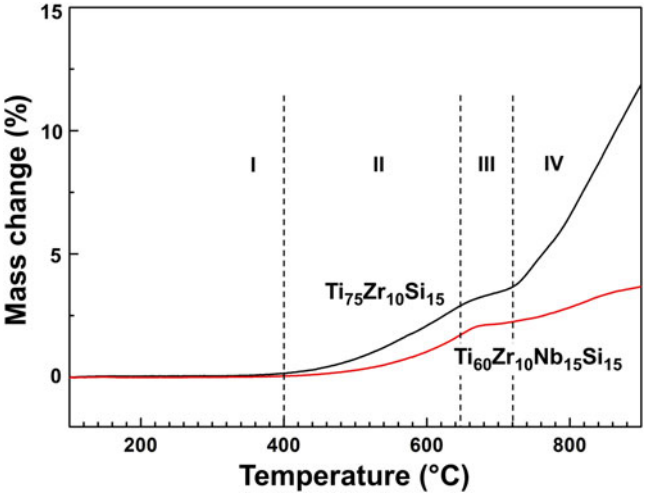

FIG. 2. Dynamic TGA curves of $Ti_{75}Zr_{10}Si_{15}$ and $Ti_{60}Zr_{10}Nb_{15}Si_{15}$ melt-spun ribbons recorded at a constant heating rate of 10 °C/min in synthetic air.

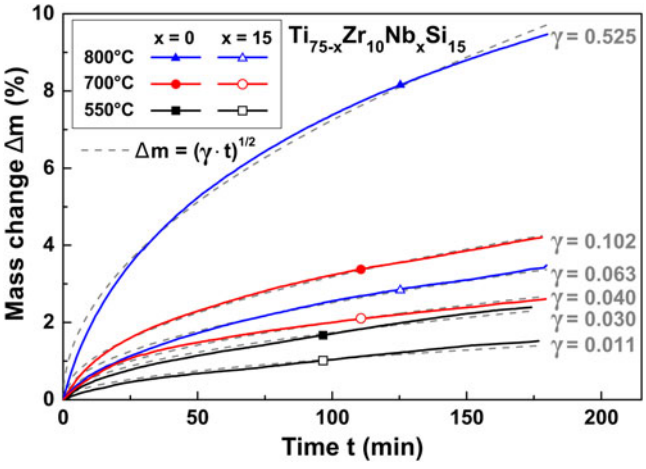

FIG. 3. Isothermal TGA curves of $Ti_{75}Zr_{10}Si_{15}$ and of $Ti_{60}Zr_{10}Nb_{15}Si_{15}$ melt-spun ribbons recorded at different temperatures for 3 h in synthetic air. The best fitting parabolic curve is shown for each condition by grey dashes.

Typical curves of the mass change of the samples as a function of time at 550, 700, and 800 °C can be seen in Fig. 3 for both alloys. In all cases, the mass change Δm approximately follows a parabolic growth law $\Delta m = (\gamma t)^{1/2}$, where γ denotes the parabolic rate constant and t the duration of the oxidative treatment. This behavior is indicative for a diffusion controlled oxidation mechanism.[28,29] By increasing the annealing temperature the mass change and consequently, the oxide growth rate rises. Comparing the responses of $Ti_{60}Zr_{10}Nb_{15}Si_{15}$ with those of $Ti_{75}Zr_{10}Si_{15}$ reveals that the quaternary alloy shows at all temperatures a lower mass increase than the ternary one. This trend is in good agreement with the dynamic TGA curves and indicates that Nb retards the oxidation process.

Although a full understanding of the Nb effect is still missing there are some proposed mechanisms that may partially explain it. Reported results of other studies about the effect of Nb on the oxidation of Ti and some Ti-based alloys can be shortly stated as: (1) doping of Ti with Nb and partially replacing Ti^{4+} with Nb^{5+} ions in the TiO_2 lattice leads to a decrease of the number of oxygen vacancies, which consequently slows down the diffusion of oxygen.[27,30,31] (2) In Ti–Nb based alloys, instead of the simple oxides TiO_2 and NbO_2 a class of complex oxides with the general formula $(Ti_xNb_{1-x})O_2$ forms by oxidation. These compounds exhibit a tetragonal rutile structure with complete miscibility.[32] The partial substitution of Ti by Nb inhibits the oxidation relative to pure Ti leading to the reduced mass increase in the quaternary alloy.

XRD patterns of samples isothermally treated for 3 h at temperatures which were selected based on the dynamic TGA curves (Fig. 2) are shown in Fig. 4. It can be seen that the patterns of $Ti_{75}Zr_{10}Si_{15}$ samples treated at 350 °C (region I) and 550 °C (region II) and the patterns of $Ti_{60}Zr_{10}Nb_{15}Si_{15}$ samples treated at 350 °C (region I), 550 °C (region II), and 700 °C (region III) are similar to those of the as-cast ribbons.[7] They comprise a sharp peak at ~45° superimposed on a diffuse halo. Therefore, it is concluded that they have a similar phase constitution, i.e., a nanocrystalline phase identified as bcc β-Ti(Nb), dispersed within a main glassy matrix phase. There is no indication for the presence of oxide phases. For the ternary alloy, the XRD pattern taken after treatment at 700 °C and for the quaternary alloy after treatment at 800 °C reveal the beginning of crystallization. When the temperature is increased to 1000 °C, a multiphase crystalline structure evolves. Both XRD patterns contain reflections of TiO_2 (rutile) and most of the remaining nonrutile reflections closely correspond to the intermetallic phase $(Ti,Zr)_5Si_3$. In addition to these phases, β-Ti (Nb) was identified in the XRD pattern of $Ti_{60}Zr_{10}Nb_{15}Si_{15}$. The metallic phases formed by crystallization of the glassy precursor in this work are thus

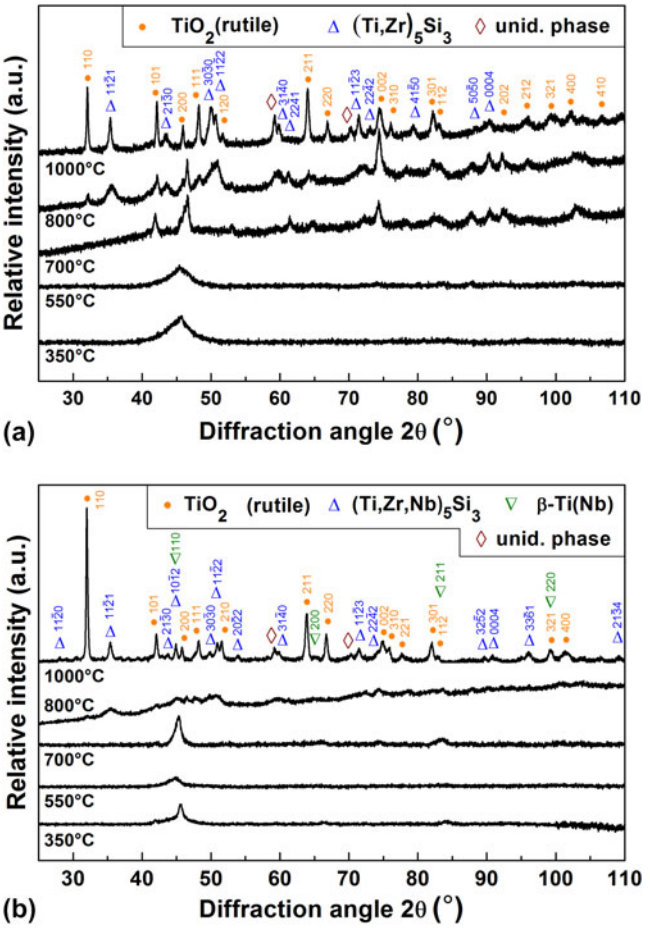

FIG. 4. XRD patterns of (a) $Ti_{75}Zr_{10}Si_{15}$ and (b) $Ti_{60}Zr_{10}Nb_{15}Si_{15}$ melt spun ribbons after isothermal TGA treatments at 350, 550, 700, 800 and 1000 °C.

identical to those found in crystalline rod samples that were cast under inert conditions.[7] For both ribbon types the highest valence oxide (TiO_2) is suggested to cover their surfaces as main oxide phase. In case of the quaternary alloy, some Ti in the oxide is likely to be replaced by Nb corresponding to the formula $(Ti_xNb_{1-x})O_2$. It was reported that these compounds exhibit a tetragonal rutile structure with full miscibility regarding Ti and Nb.[32]

Figure 5 shows SEM micrographs of sample surfaces of both alloy types after oxidation at 550, 700, and 800 °C for 3 h in synthetic air. For both alloys, at 550 °C no oxide film related contrast is clearly visible in the SEM images. A thin oxide layer, which is relatively smooth, forms. Upon increasing the temperature to 700 °C, the oxide grains grow and the film thickens. After treatment at 800 °C, the surface is covered with larger oxides and the oxide grain growth rises dramatically in particular for the ternary alloy. This is in good agreement with the results of TGA analysis which revealed a rapid mass increase due to oxidation at

temperatures ≥800 °C. The observed more retarded oxide grain growth on the quaternary alloy is also in accordance with TGA results and confirms again the Nb effect which was discussed above.

As the morphology of the oxide films on the samples oxidized at 550 °C had a rather smooth appearance AFM was applied to study the surface morphology at nanoscale resolution and to analyze the surface roughness of the samples. The results of a statistical analysis, which gives root mean squared (r.m.s.) roughness values are reported in Table I. It can be seen that the presence of the metal oxides on the treated surfaces increases the roughness in comparison with the not treated ribbons by a factor of almost 2. The amount of the formed nuclei and the growth rate of the oxide grains define the values of available surface area (surface roughness) of the oxidized samples.

This thermal analysis surface morphology study suggests that once the ribbon samples are in contact with

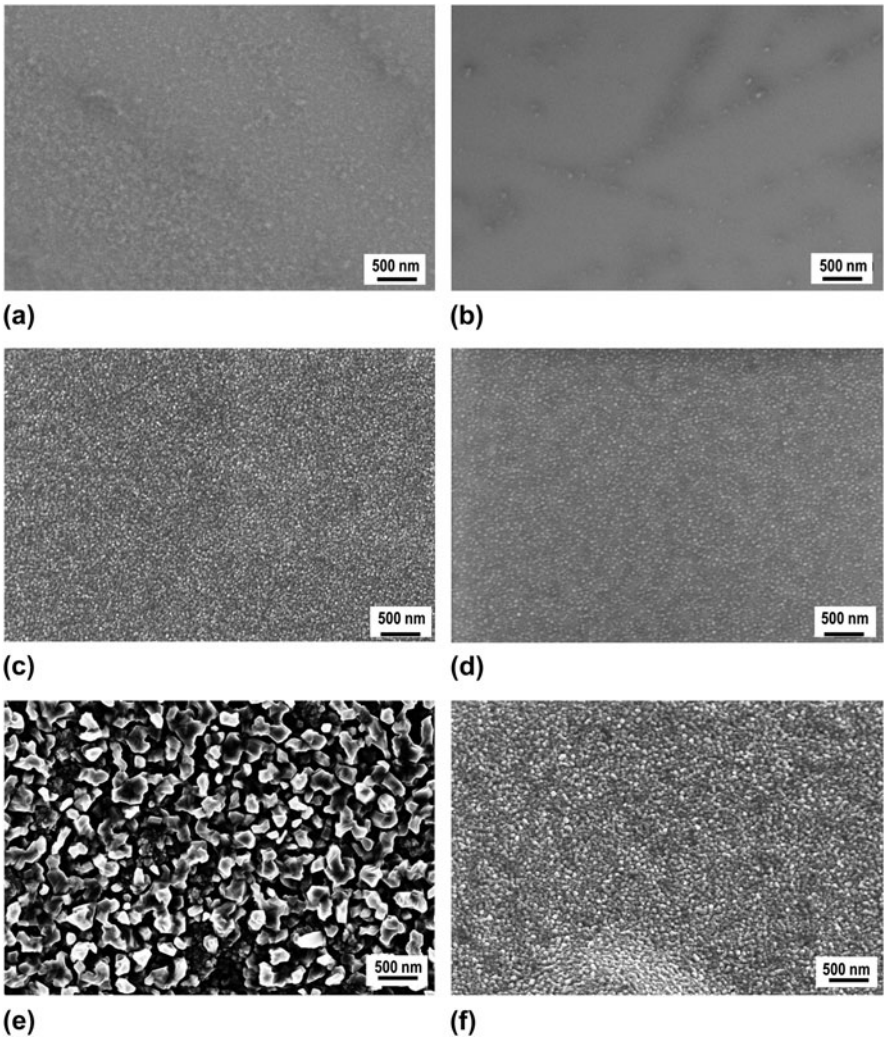

FIG. 5. Scanning electron micrographs showing surface morphologies (a, c and e) of $Ti_{75}Zr_{10}Si_{15}$ and (b, d and f) of $Ti_{60}Zr_{10}Nb_{15}Si_{15}$ melt-spun ribbons oxidized at (a and b) 550 °C, (c and d) 700 °C and (e and f) 800 °C for 3 h in synthetic air.

TABLE I. R.m.s. roughness values (obtained by AFM, scanned area: 15 × 15 μm), surface microhardness (Vickers indenter: 10 gf applied load) and contact angle values for $Ti_{75}Zr_{10}Si_{15}$ and $Ti_{60}Zr_{10}Nb_{15}Si_{15}$ ribbons (air-sides) as-spun and thermally oxidized at 550 °C for 3 h.

	R.m.s. roughness (nm)		Microhardness ($HV_{0.01}$)		Contact angle (°)	
Alloy	As-spun	Treated	As-spun	Treated	As-spun	Treated
$Ti_{75}Zr_{10}Si_{15}$	1.4 ± 0.2	2.4 ± 0.2	602 ± 21	1285 ± 89	85 ± 2	73 ± 2
$Ti_{60}Zr_{10}Nb_{15}Si_{15}$	1.0 ± 0.2	2.0 ± 0.2	601 ± 36	1287 ± 91	92 ± 2	74 ± 2

oxygen at elevated temperatures above 400 °C, the nucleation of oxides occurs throughout the whole surface. Initial formation of a thin, rather smooth oxide scale is followed by agglomeration processes and growth of single oxide grains which cover the surface at the end completely. The kinetics of oxide film thickening and grain growth is not only determined by the annealing temperature but also by the alloy composition whereby Nb has a particular retarding effect.

C. Detailed investigation of melt-spun ribbons oxidized at 550 °C for 3 h

In the previous investigations, the melt-spun metastable Ti–Zr–(Nb)–Si alloys were found to preserve their glass–matrix nanocomposite microstructure without any significant crystallization only at temperatures below the onset of the second crystallization event, i.e., below T_{x2} = 590 °C for the ternary and T_{x2} = 632 °C for the quaternary alloy (see DSC data in Fig. 1). On the other hand, significant oxidation rates were observed for both alloys only at temperatures above 400 °C (Fig. 2). Therefore, for biomedical surface modification applications, only thermal oxidation treatments in this temperature window are useful. In the following, the oxidation states on the melt-spun ternary and quaternary alloy surfaces, obtained after thermal treatment at 550 °C for 3 h in synthetic air were characterized in more detail using high resolution methods.

1. TEM studies

The structure and thickness of the oxide films have been investigated by TEM and EDX spectroscopy. In Fig. 6, scanning TEM (STEM) and high resolution images of cross sectional regions of thermally oxidized $Ti_{75}Zr_{10}Si_{15}$ (a and b) and $Ti_{60}Zr_{10}Nb_{15}Si_{15}$ (c and d) surfaces are shown. In the STEM images of both alloy samples, three regions are observed. The EDX results reveal that the dark regions (I and II) correspond to the oxides and the bright region to the alloy substrate. The average chemical composition of the oxide layers measured by EDX for the treated $Ti_{75}Zr_{10}Si_{15}$ ribbon is Ti = 30 at.%, O = 61 at.%, Zr = 4 at.%, Si = 5 at.% for region (I) and Ti = 35 at.%, O = 48 at.%, Zr = 7 at.%, Si = 10 at.% for region (II). According to the EDX analysis, the outer region of the oxide mainly consists of TiO_2 while in the inner region a decreasing O/Ti ratio indicates the presence of TiO or Ti_2O_3 as well. For the treated $Ti_{60}Zr_{10}Nb_{15}Si_{15}$ alloy, EDX revealed a similar trend as for the ternary alloy. In addition, the existence of other alloying element species (Zr, Si, Nb) in the oxide layer regions is observed. The film thickness is estimated as ~560 nm for $Ti_{75}Zr_{10}Si_{15}$ and ~460 nm for $Ti_{60}Zr_{10}Nb_{15}Si_{15}$ confirming the reduced thickness growth when Nb species are present. The oxide layers have been investigated by high resolution TEM and representative images of the outer regions are shown in Figs. 6(b) and 6(d) revealing mainly an amorphous structure [confirmed by the SAED diffraction pattern, inset of Figs. 6(b) and 6(d)]. That can explain why only a featureless surface coverage was observed by SEM in top view (Fig. 5).

2. AES investigations

For further detailed compositional characterization of the oxide films that form on the glass-forming Ti–Zr–(Nb)–Si alloys under thermal oxidation conditions, AES sputter depth-profiling was conducted. Figure 7 summarizes exemplarily depth profiles of $Ti_{75}Zr_{10}Si_{15}$ and $Ti_{60}Zr_{10}Nb_{15}Si_{15}$ sample surfaces thermally oxidized at 550 °C for 3 h. Due to the high thickness of the oxide film, two sputtering rates have been applied. For the first 3 to 5 min, a sputter rate of 6.6 nm/min was used [Figs. 7(a) and 7(c)]. Then, for the following 90 min, a sputter rate of 17 nm/min (determined in SiO_2) [Figs. 7(b) and 7(d)] was used. The AES profiles of the surface regions of both alloy samples reveal that all constituent element species are present in the oxide layers. They consist mainly of Ti oxide with some contribution of the other elements. Within the first 60 seconds of sputtering, the Si concentration is higher than that of other elements, indicating the presence of a very thin Si oxide-rich film (about 6.6 nm) in the outermost zone which was not detected by XRD or TEM. According to thermodynamic aspects, SiO_2 has a larger negative formation enthalpy in comparison with the other constituent oxides; so the driving force for SiO_2 oxide formation is smaller but its growth kinetic is obviously faster.[26]

By increasing the total sputter time to about 35 min, the oxygen signal decayed to the half width value between maximum and minimum value which was defined as oxide/metal interface. Considering the different sputter rates and the corresponding times, the oxide thickness on the ternary alloy is estimated to be ~560 nm. For the quaternary alloy sample, the film thickness decreases to ~465 nm. It can be seen that the determined film thickness values for $Ti_{75}Zr_{10}Si_{15}$ and $Ti_{60}Zr_{10}Nb_{15}Si_{15}$ are in good agreement with those estimated from TEM. No sharp decay of the oxygen concentration can be perceived, which points to a higher roughness of the oxides in the investigated region.

3. Microhardness

A high hardness of implant surfaces is mandatory to reduce wear rates especially in articulation joint applications. The measured microhardness values of as-spun and thermally oxidized samples (airside of ribbons) are given

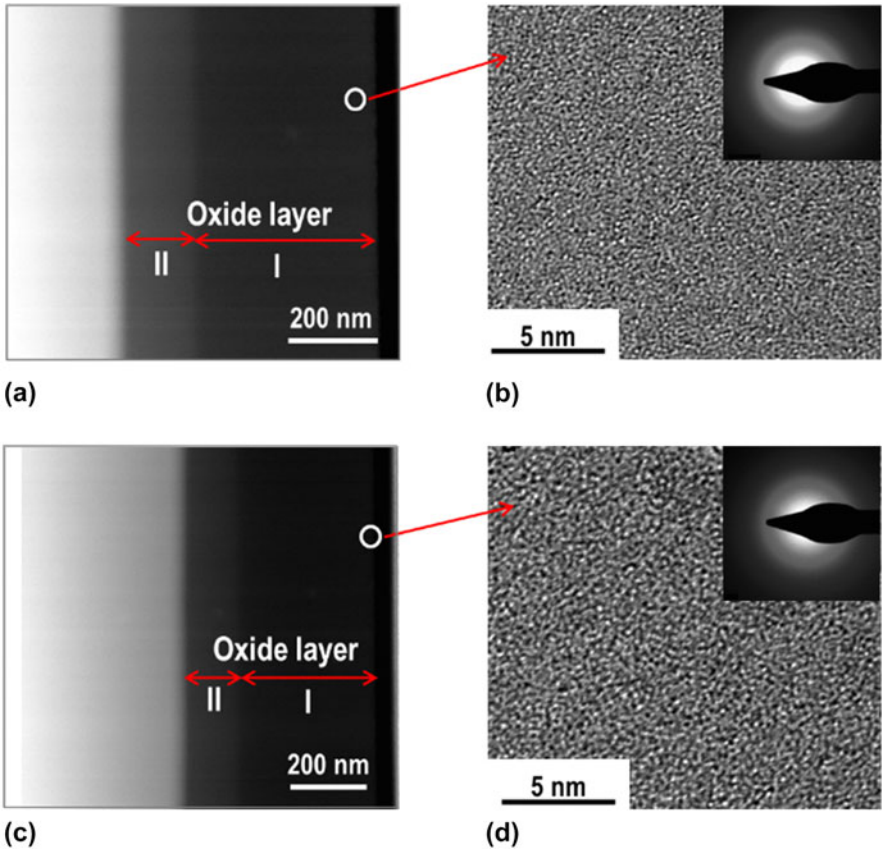

FIG. 6. (a) STEM, (b) high resolution TEM micrograph of the $Ti_{75}Zr_{10}Si_{15}$ and (c) STEM, (d) high resolution TEM micrograph of the $Ti_{60}Zr_{10}Nb_{15}Si_{15}$ ribbon; the ribbons are thermally oxidized at 550 °C for 3 h.

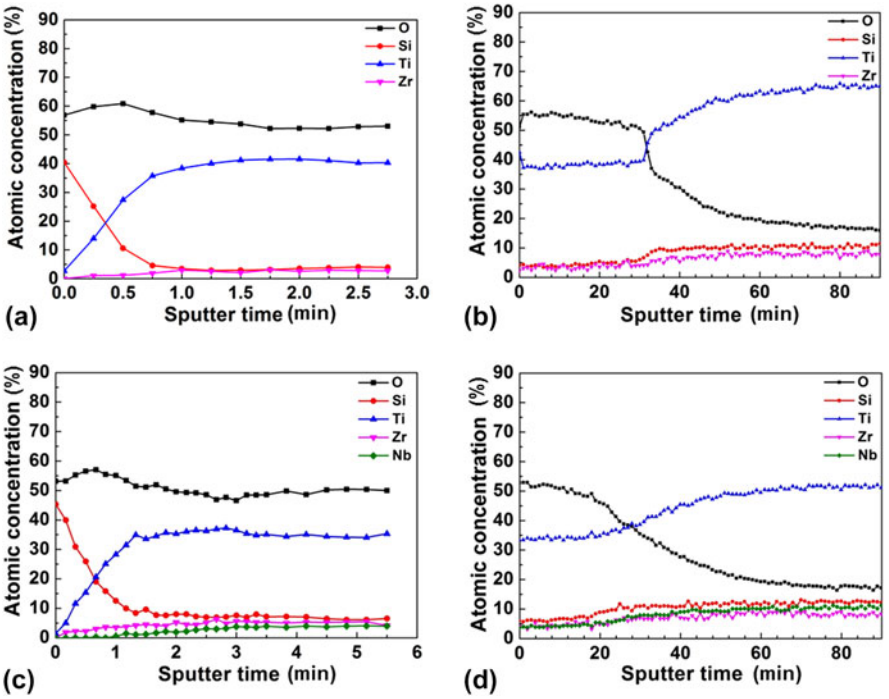

FIG. 7. Elemental concentration sputter depth profiles obtained from AES measurements at surfaces (airside) of $Ti_{75}Zr_{10}Si_{15}$ for different sputter depths (a) in a surface region (first 2.7 min sputtering = 18 nm depth) and (b) the subsequent bulk-near region (following 90 min sputtering = 1500 nm). For $Ti_{60}Zr_{10}Nb_{15}Si_{15}$ ribbons similar results are shown (c) for the first 36 nm and (d) the following 1500 nm.

in Table I. A constant load of 10 g for a holding time of 10 s (which provides a depth of about 1 μm) has been applied to be able to evaluate mainly the effect of the surface oxide layer (~500–600 nm) on the hardness. The microhardness values of as-spun $Ti_{75}Zr_{10}Si_{15}$ and $Ti_{60}Zr_{10}Nb_{15}Si_{15}$ samples are 690 and 691 $HV_{0.01}$, respectively. The thermally oxidized samples reveal a significant increase in hardness by about two times due to the formation of thicker oxide layers. The higher scattering of values for treated samples may be due to the increased surface roughness.

4. Wettability

When a biomaterial is implanted into a biological system, the first and the foremost event is the wetting of the implant material by the physiological fluids. This further determines the adsorption degree of specific proteins which in turn mediate the recruitment and activation of cells and the stimulation of new tissue development.[33]

Surface roughness and surface free energy are important parameters determining the wettability of solid surfaces. The presence of metal oxides on the surface of metallic samples affects both parameters and, as a consequence, the wettability of the samples.[21] In the present study the surface contact angle was evaluated by sessile drop measurements of distilled water at room temperature and the results are summarized in Table I together with surface roughness data obtained by means of AFM. It can be seen that contact angles for as-spun samples of ternary and quaternary alloys are in the same range of 85–92° which indicates hydrophobicity. Both as-spun surface states are very smooth according to rather low measured surface roughness values. Most importantly, for both metallic glass substrates the oxides which were formed by thermal treatment at 550 °C reduced the contact angle values, i.e., by about 14% for $Ti_{75}Zr_{10}Si_{15}$ and 19% for $Ti_{60}Zr_{10}Nb_{15}Si_{15}$. But amorphous oxide formation under these conditions was only related with marginal increase of the surface roughness. Therefore, it can be concluded that the thermal oxidative treatment yields a tendency towards improved wettability of the alloy surfaces and this must be mainly due to the changes of surface chemistry. In an earlier study, Patel et al.[21] conducted contact angle measurements with distilled water on surfaces of Ti–6Al–4V for bio-implant applications and they observed the same principal trend. The hydrophobicity of as-ground alloy states was explained by the high surface free energy barrier of the valve-metal alloy constituents. After thermal oxidation, the polarity

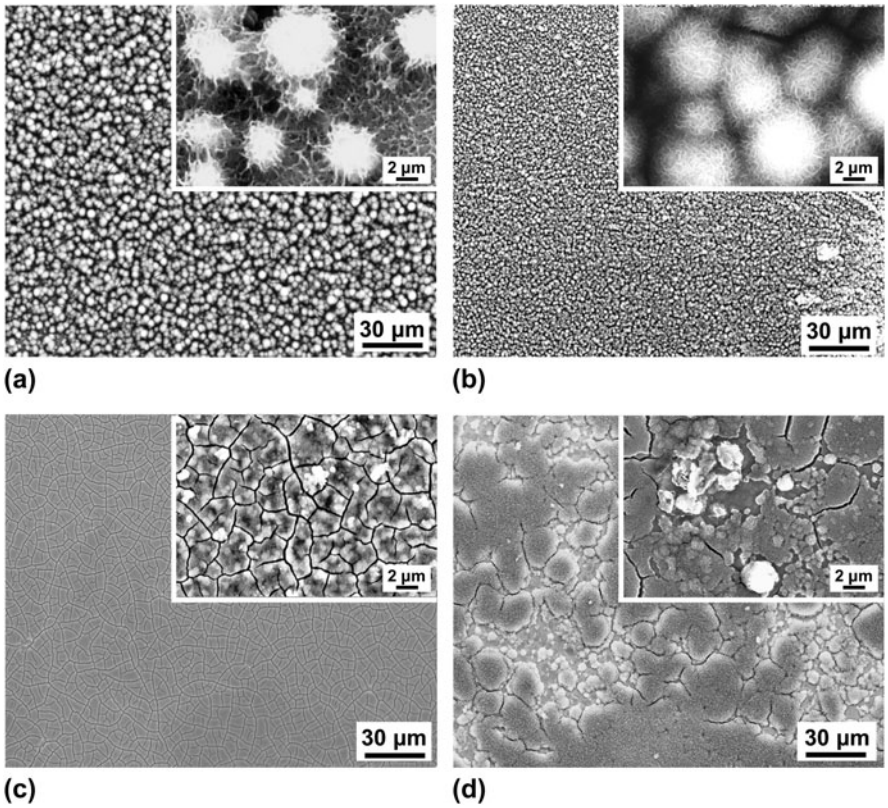

FIG. 8. SEM images of surfaces of untreated and thermally oxidized $Ti_{75}Zr_{10}Si_{15}$ and $Ti_{60}Zr_{10}Nb_{15}Si_{15}$ ribbon samples (air-side) treated with NaOH and immersed in SBF solution for 10 days: (a) untreated $Ti_{75}Zr_{10}Si_{15}$ and (b) thermally oxidized $Ti_{75}Zr_{10}Si_{15}$, (c) untreated $Ti_{60}Zr_{10}Nb_{15}Si_{15}$ and (d) thermally oxidized $Ti_{60}Zr_{10}Nb_{15}Si_{15}$.

and surface free energy state is significantly changed. The oxide species have the ability to easily split water, thereby forming hydroxylgroups on the surface that can attract water molecules making the surface more hydrophilic. On Ti–6Al–4V coarse crystalline anatase and rutile type oxides formed which caused a strong hydrophilicity corresponding to contact angles of only 5°. In contrast, this effect was much less pronounced for thermally treated Ti–Zr–Si(–Nb) metallic glass alloy samples which may be ascribed to the amorphous nature of the oxides as well to a different oxide compositions.

5. SBF test (apatite-forming ability)

The analysis of hydroxyapatite formation on a material in a SBF solution may be used as a preliminary in vitro assessment of the bone forming bioactivity of that material.[25] In a previous study, the ability of the melt-spun $Ti_{75}Zr_{10}Si_{15}$ and $Ti_{60}Zr_{10}Nb_{15}Si_{15}$ alloys to generate hydroxyapatite at their surface (air-sides of ribbon samples) was tested.[6] It was concluded, that the melt-spun $Ti_{75}Zr_{10}Si_{15}$ alloy has an apatite-forming ability similar to that of cp-Ti. For the melt-spun $Ti_{60}Zr_{10}Nb_{15}Si_{15}$ alloy, the formation of hydroxyapatite is retarded, suggesting that additions of Nb inhibit the apatite-forming ability of Ti-based alloys. This is in agreement with previous studies on β-phase alloys which also revealed a reduced rate of the apatite-forming ability when adding 45 wt% Nb to pure Ti.[34]

In the present study, SBF tests have been also conducted on $Ti_{75}Zr_{10}Si_{15}$ and $Ti_{60}Zr_{10}Nb_{15}Si_{15}$ ribbons which were thermally oxidized at 550 °C for 3 h. Similarly to the untreated ribbons,[6] the thermally oxidized samples were immersed in SBF solution for 10 days and their surface was investigated by SEM and EDX. In Fig. 8, selected SEM images are shown. They indicate that on the $Ti_{75}Zr_{10}Si_{15}$ surfaces due to overlapping of hemispherical growth centers, highly porous layers developed. The layers on the $Ti_{60}Zr_{10}Nb_{15}Si_{15}$ surfaces exhibited relatively smoother scale-like morphologies. In comparison to the thermally untreated surface states, the thermally treated surface states in [Figs. 8(b) and 8(d)] were covered with a quite compact layer (already after 10 days of immersion). EDX confirms the presence of Ca and P in these layers on all four substrate types indicating that they contain Ca–phosphate compounds. These layers have a typical thickness of a few micrometers and their morphology hints to hydroxyapatite as frequently observed in the literature.[25] However, while it is obvious from SEM images in Fig. 8 that the presence of Nb in the metallic glass retards the coating formation, differences between untreated and thermally treated surface states regarding Ca/P ratios (indicating the type of Ca–phosphate) or coating thicknesses are not so clear. From SEM observations of multiple samples a trend can be derived that on thermally treated alloy surfaces, the precipitated coatings are more compact and dense over the whole exposed substrate surface.

IV. CONCLUSIONS

It has been demonstrated that thermal oxidation, which is one of the most effective surface modification methods established for commercial Ti-based implant materials, can be well applied to melt-spun glass-matrix nanocomposite $Ti_{75}Zr_{10}Si_{15}$ and $Ti_{60}Zr_{10}Nb_{15}Si_{15}$ alloys. This treatment aims at formation of Ti oxide-based layers to improve the surface biocompatibility. Oxidation rates significantly increased at temperatures ≥400 °C, where oxide formation approximately follows a parabolic growth law. Partial substitution of Ti by Nb in the initial alloy composition retards the oxidation process at a given temperature. At temperatures >590 °C, surface oxidation superimposes significant crystallization events. Therefore, surface modification by thermal oxidation is only feasible in the temperature window 400 °C $< T_{\text{oxidation}} <$ 590 °C.

Ribbon samples of the ternary and the quaternary alloy, which were exposed at 550 °C to synthetic air for up to 3 h, formed compact amorphous oxide layers on their surfaces with thicknesses of ~560 and ~460 nm, respectively. A gradient in the chemical composition of the oxide layers throughout their depth was detected. These layers are composed mainly of Ti-oxides, but comprise also species of all alloy constituents, in particular, SiO_2 in their outermost regions. During the abovementioned preliminary tests, the oxidized alloy samples showed suitable fundamental properties for implant applications, i.e., high hardness, good wettability, and the formation of Ca- and P-containing coatings exhibiting typical morphologies of apatite after 10 days of immersion in SBF solution.

ACKNOWLEDGMENTS

The authors thank S. Donath for sample preparation, C. Geringswald for thermogravimetric experiments, B. Bartusch for DSC measurements, A. Voβ for SBF testing and S. Kaschube for AES measurements. Funding by the European Commission within the framework of the FP7-MCITN network BioTiNet (PITN-GA-2010-264635) is gratefully acknowledged.

REFERENCES

1. C. Suryanarayana and A. Inoue: *Bulk metallic glasses* (CRC Press, Boca Raton, 2011).
2. J.-J. Oak, D.V. Louzguine-Luzgin, and A. Inoue: Investigation of glass-forming ability, deformation and corrosion behavior of Ni-free Ti-based BMG alloys designed for application as dental implants. *Mater. Sci. Eng., C* **29**, 322 (2009).

3. J.J. Oak, D.V. Louzguine-Luzgin, and A. Inoue: Fabrication of Ni-free Ti-based bulk-metallic glassy alloy having potential for application as biomaterial, and investigation of its mechanical properties, corrosion, and crystallization behavior. *J. Mater. Res.* **22**, 1346 (2007).
4. F. Qin, X. Wang, S. Zhu, A. Kawashima, K. Asami, A. Inoue: Fabrication, and corrosion property of novel Ti-based bulk glassy alloys without Ni. *Mater. Trans.* **48**, 515 (2007).
5. M. Calin, A. Gebert, A.C. Ghinea, P.F. Gostin, S. Abdi, C. Mickel, and J. Eckert: Designing biocompatible Ti-based metallic glasses for implant applications. *Mater. Sci. Eng., C* **33**, 875 (2013).
6. S. Abdi, S. Oswald, P.F. Gostin, A. Helth, J. Sort, M.D. Baró, M. Calin, L. Schultz, J. Eckert, and A. Gebert: Designing new biocompatible glass-forming $Ti_{75-x}Zr_{10}Nb_xSi_{15}$ (x = 0, 15) alloys: Corrosion, passivity, and apatite formation. *J. Biomed. Mater. Res., Part B* **104B**, 27–38 (2015).
7. S. Abdi, M.S. Khoshkhoo, O. Shuleshova, M. Bönisch, M. Calin, L. Schultz, J. Eckert, M.D. Baró, J. Sort, and A. Gebert: Effect of Nb addition on microstructure evolution and nanomechanical properties of a glass-forming Ti–Zr–Si alloy. *Intermetallics* **46**, 156 (2014).
8. F. Variola, F. Vetrone, L. Richert, P. Jedrzejowski, J.H. Yi, S. Zalzal, S. Clair, A. Sarkissian, D.F. Perepichka, J.D. Wuest, F. Rosei, and A. Nanci: Improving Biocompatibility of implantable metals by Nanoscale modification of Surfaces: An Overview of Strategies, fabrication methods, and Challenges. *Small* **5**, 996 (2009).
9. X. Liu, P.K. Chu, and C. Ding: Surface modification of titanium, titanium alloys, and related materials for biomedical applications. *Mater. Sci. Eng., R* **47**, 49 (2004).
10. S. Kumar, T.S.N. Sankara Narayanan, S. Ganesh Sundara Raman, and S.K. Seshadri: Thermal oxidation of Ti6Al4V alloy: Microstructural and electrochemical characterization. *Mater. Chem. Phys.* **119**, 337 (2010).
11. M. Long and H.J. Rack: Titanium alloys in total joint replacement—a materials science perspective. *Biomaterials* **19**, 1621 (1998).
12. P.A. Dearnley: A review of metallic, ceramic and surface-treated metals used for bearing surfaces in human joint replacements. *Proc. Inst. Mech. Eng., Part H* **213**, 107 (1999).
13. S. Minagar, C.C. Berndt, J. Wang, E. Ivanova, and C. Wen: A review of the application of anodization for the fabrication of nanotubes on metal implant surfaces. *Acta Biomater.* **8**, 2875 (2012).
14. T. Hanawa: Research and development of metals for medical devices based on clinical needs. *Sci. Technol. Adv. Mater.* **13**, 064102 (2012).
15. S. Kumar, T. Narayanan, S.G.S. Raman, and S.K. Seshadri: Thermal oxidation of CP-Ti: Evaluation of characteristics and corrosion resistance as a function of treatment time. *Mater. Sci. Eng., C* **29**, 1942 (2009).
16. M.C. Garcia-Alonso, L. Saldana, G. Valles, J.L. Gonzalez-Carrasco, J. Gonzalez-Cabrero, M.E. Martinez, E. Gil-Garay, and L. Munuera: In vitro corrosion behaviour and osteoblast response of thermally oxidised Ti6Al4V alloy. *Biomaterials* **24**, 19 (2003).
17. S. Kumar, T. Narayanan, S.G.S. Raman, and S.K. Seshadri: Thermal oxidation of CP Ti—An electrochemical and structural characterization. *Mater. Charact.* **61**, 589 (2010).
18. S. Kumar, T.S.N.S. Narayanan, and S. Ganesh Sundara Raman, and S.K. Seshadri: Surface modification of CP-Ti to improve the fretting-corrosion resistance: Thermal oxidation vs. anodizing. *Mater. Sci. Eng., C* **30**, 921 (2010).
19. M.F. Lopez, J.A. Jimenez, and A. Gutierrez: Corrosion study of surface-modified vanadium-free titanium alloys. *Electrochim. Acta* **48**, 1395 (2003).
20. H. Ahn, D. Lee, K.-M. Lee, K. Lee, D. Baek, and S.-W. Park: Oxidation behavior and corrosion resistance of Ti–10Ta–10Nb alloy. *Surf. Coat. Technol.* **202**, 5784 (2008).
21. S.B. Patel, A. Hamlekhan, D. Royhman, A. Butt, J. Yuan, T. Shokuhfar, C. Sukotjo, M.T. Mathew, G. Jursich, and C.G. Takoudis: Enhancing surface characteristics of Ti–6Al–4V for bio-implants using integrated anodization and thermal oxidation. *J. Mater. Chem. B* **2**, 3597 (2014).
22. V. Sollazzo, F. Pezzetti, A. Scarano, A. Piattelli, L. Massari, G. Brunelli, and F. Carinci: Anatase coating improves implant osseointegration in vivo. *J. Craniofac. Surg.* **18**, 806 (2007).
23. J. Forsgren, S. Svahn, T. Jarmar, and H. Engqvist: Formation and adhesion of biomimetic hydroxyapatite deposited on titantium substrates. *Acta Biomater.* **3**, 980 (2007).
24. S. Oswald, P.-F. Gostin, A. Helth, S. Abdi, L. Giebeler, H. Wendrock, M. Calin, J. Eckert, and A. Gebert: Xps and AES sputter-depth profiling at surfaces of biocompatible passivated Ti-based alloys: Concentration quantification considering chemical effects. *Surf. Interface Anal.* **46**, 683 (2014).
25. T. Kokubo and H. Takadama: How useful is SBF in predicting in vivo bone bioactivity?. *Biomaterials* **27**, 2907 (2006).
26. J.D. Cox, D.D. Wagman, and V.A. Medvedev, eds.: *Key values for thermodynamics* (Hemisphere Publishing Co., New York, 1989).
27. M. Metikos-Huković, A. Kwokal, and J. Piljac: The influence of niobium and vanadium on passivity of titanium-based implants in physiological solution. *Biomaterials* **24**, 3765 (2003).
28. P. Gabbott, ed.: *Principles and applications of thermal analysis* (Blackwell Publishing Ltd., Oxford, 2008).
29. B.E. Deal and A.S. Grove: General relationship for the thermal oxidation of silicon. *J. Appl. Phys.* **36**, 3770 (1965).
30. P. Perez, V.A.C. Haanappel, and M.F. Stroosnijder: The effect of niobium on the oxidation behaviour of titanium in N_2/20% O_2 atmospheres. *Mater. Sci. Eng., A* **284**, 126 (2000).
31. T.K. Roy, R. Balasubramaniam, and A. Ghosh: High-temperature oxidation of Ti3Al-based titanium aluminides in oxygen. *Metall. Mater. Trans. A* **27**, 3993 (1996).
32. M.N. Armenise, C. Canali, M. DeSario, A. Carnera, P. Mazzoldi, and G. Celotti: Characterization of TiO_2, $LiNb_3O_8$, and $(Ti_{0.65}Nb_{0.35})O_2$ compound growth observed during Ti:$LiNbO_3$ optical waveguide fabrication. *J. Appl. Phys.* **54**, 6223 (1983).
33. J. Nychka and M. Gentleman: Implications of wettability in biological materials science. *JOM* **62**, 39 (2010).
34. P.F. Gostin, A. Helth, A. Voss, R. Sueptitz, M. Calin, J. Eckert, and A. Gebert: Surface treatment, corrosion behavior, and apatite-forming ability of Ti–45Nb implant alloy. *J. Biomed. Mater. Res., Part B* **101B**, 269 (2013).